DIGITAL ACCESS TO SCHOLARSHIP AT HARVARD
DASH.HARVARD.EDU

HARVARD LIBRARY
Office for Scholarly Communication

Motion microscopy for visualizing and quantifying small motions

The Harvard community has made this article openly available. **Please share** how this access benefits you. Your story matters

Citation	Wadhwa, N., J. G. Chen, J. B. Sellon, D. Wei, M. Rubinstein, R. Ghaffari, D. M. Freeman, et al. 2017. "Motion microscopy for visualizing and quantifying small motions." Proceedings of the National Academy of Sciences of the United States of America 114 (44): 11639-11644. doi:10.1073/pnas.1703715114. http://dx.doi.org/10.1073/pnas.1703715114.
Published Version	doi:10.1073/pnas.1703715114
Citable link	http://nrs.harvard.edu/urn-3:HUL.InstRepos:34493366
Terms of Use	This article was downloaded from Harvard University's DASH repository, and is made available under the terms and conditions applicable to Other Posted Material, as set forth at http://nrs.harvard.edu/urn-3:HUL.InstRepos:dash.current.terms-of-use#LAA

Motion microscopy for visualizing and quantifying small motions

Neal Wadhwa[a,1], Justin G. Chen[a,b], Jonathan B. Sellon[c,d], Donglai Wei[a], Michael Rubinstein[e], Roozbeh Ghaffari[d], Dennis M. Freeman[c,d,f], Oral Büyüköztürk[b], Pai Wang[g], Sijie Sun[g], Sung Hoon Kang[g,h,i], Katia Bertoldi[g], Frédo Durand[a,f], and William T. Freeman[a,e,f,2]

[a]Computer Science and Artificial Intelligence Laboratory, Massachusetts Institute of Technology, Cambridge, MA 02139; [b]Department of Civil and Environmental Engineering, Massachusetts Institute of Technology, Cambridge, MA 02139; [c]Harvard-MIT Program in Health Sciences and Technology, Cambridge, MA 02139; [d]Research Laboratory of Electronics, Massachusetts Institute of Technology, Cambridge, MA 02139; [e]Google Research, Google Inc. Cambridge, MA 02139; [f]Department of Electrical Engineering and Computer Science, Massachusetts Institute of Technology, Cambridge, MA 02139; [g]School of Engineering and Applied Sciences, Harvard University, Cambridge, MA 02138; [h]Department of Mechanical Engineering, Johns Hopkins University, Baltimore, MD 21218; and [i]Hopkins Extreme Materials Institute, Johns Hopkins University, Baltimore, MD 21218

Although the human visual system is remarkable at perceiving and interpreting motions, it has limited sensitivity, and we cannot see motions that are smaller than some threshold. Although difficult to visualize, tiny motions below this threshold are important and can reveal physical mechanisms, or be precursors to large motions in the case of mechanical failure. Here, we present a "motion microscope," a computational tool that quantifies tiny motions in videos and then visualizes them by producing a new video in which the motions are made large enough to see. Three scientific visualizations are shown, spanning macroscopic to nanoscopic length scales. They are the resonant vibrations of a bridge demonstrating simultaneous spatial and temporal modal analysis, micrometer vibrations of a metamaterial demonstrating wave propagation through an elastic matrix with embedded resonating units, and nanometer motions of an extracellular tissue found in the inner ear demonstrating a mechanism of frequency separation in hearing. In these instances, the motion microscope uncovers hidden dynamics over a variety of length scales, leading to the discovery of previously unknown phenomena.

visualization | motion | image processing

Motion microscopy is a computational technique to visualize and analyze meaningful but small motions. The motion microscope enables the inspection of tiny motions as optical microscopy enables the inspection of tiny forms. We demonstrate its utility in three disparate problems from biology and engineering: visualizing motions used in mammalian hearing, showing vibration modes of structures, and verifying the effectiveness of designed metamaterials.

The motion microscope is based on video magnification (1–4), which processes videos to amplify small motions of any kind in a specified temporal frequency band. We extend the visualization produced by video magnification to scientific and engineering analysis. In addition to visualizing tiny motions, we quantify both the object's subpixel motions and the errors introduced by camera sensor noise (5). Thus, the user can see the magnified motions and obtain their values, with variances, allowing for both qualitative and quantitative analyses.

The motion microscope characterizes and amplifies tiny local displacements in a video by using spatial local phase. It does this by transforming the captured intensities of each frame's pixels into a wavelet-like representation where displacements are represented by phase shifts of windowed complex sine waves. The representation is the complex steerable pyramid (6), an overcomplete linear wavelet transform, similar to a spatially localized Fourier transform. The transformed image is a sum of basis functions, approximated by windowed sinusoids (Fig. S1), that are simultaneously localized in spatial location (x, y), scale r, and orientation θ. Each basis function coefficient gives spatially

local frequency information and has an amplitude $A_{r,\theta}(x, y)$ and a phase $\phi_{r,\theta}(x, y)$.

To amplify motions, we compute the unwrapped phase difference of each coefficient of the transformed image at time t from its corresponding value in the first frame,

$$\Delta\phi_{r,\theta}(x, y, t) := \phi_{r,\theta}(x, y, t) - \phi_{r,\theta}(x, y, 0). \quad [1]$$

We isolate motions of interest and remove components due to noise by temporally and spatially filtering $\Delta\phi_{r,\theta}$. We amplify the filtered phase shifts by the desired motion magnification factor to obtain modified phases for each basis function at each time t. We then transform back each frame's steerable pyramid to produce the motion-magnified output video (Fig. S2) (3).

We estimate motions under the assumption that there is a single, small motion at each spatial location. In this case, each coefficient's phase difference, $\Delta\phi_{r,\theta}$, is approximately equal to the dot product of the corresponding basis function's orientation and the 2D motion (7) (*Relation Between Local Phase Differences and Motions*). The reliability of spatial local phase varies across scale and orientations, in direct proportion to the coefficient's amplitude (e.g., coefficients for basis functions orthogonal to an edge are more reliable than those along it) (Fig. S3 and

Significance

Humans have difficulty seeing small motions with amplitudes below a threshold. Although there are optical techniques to visualize small static physical features (e.g., microscopes), visualization of small dynamic motions is extremely difficult. Here, we introduce a visualization tool, the motion microscope, that makes it possible to see and understand important biological and physical modes of motion. The motion microscope amplifies motions in a captured video sequence by rerendering small motions to make them large enough to see and quantifies those motions for analysis. Amplification of these tiny motions involves careful noise analysis to avoid the amplification of spurious signals. In the representative examples presented in this study, the visualizations reveal important motions that are invisible to the naked eye.
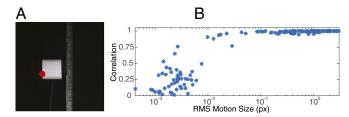
COMPUTER SCIENCES

Fig. 1. A comparison of our quantitative motion estimation vs. a laser vibrometer. Several videos of a cantilevered beam excited by a shaker were taken with varying focal length, exposure times, and excitation magnitude. The horizontal, lateral motion of the red point was also measured with a laser vibrometer. (*A*) A frame from one video. (*B*) The correlation between the two signals across the videos vs. root mean square (RMS) motion size in pixels (px). Only motions at the red point in *A* were used in our analysis. More results are in Fig. S4.

Low-Amplitude Coefficients Have Noisy Phase). We combine information about the motion from multiple orientations by solving a weighted least squares problem with weights equal to the amplitude squared. The result is a 2D motion field. This processing is accurate, and we provide comparisons to other algorithms and sensors (Fig. 1, *Synthetic Validation*, and Figs. S4 and S5).

For a still camera, the sensitivity of the motion microscope is mostly limited by local contrast and camera noise—fluctuations of pixel intensities present in all videos (5). When the video is motion-magnified, this noise can lead to spurious motions, especially at low-contrast edges and textures (Fig. S6). We measure motion noise level by computing the covariance matrix of each estimated motion vector. Estimating this directly from the input video is usually impossible, because it requires observing the motions without noise. We solve this by creating a simulated noisy video with zero motion, replicating a static frame of the input video and adding realistic, independent noise to

each frame. We compute the sample covariance of the estimated motion vectors in this simulated video (Fig. S7 and *Noise Model and Creating Synthetic Video*). We show analytically, and via experiments in which the motions in a temporal band are known to be zero, that these covariance matrices are accurate for real videos (*Analytic Justification of Noise Analysis* and Figs. S8 and S9). We also analyze the limits of our technique by comparing to a laser vibrometer and show that, with a Phantom V-10 camera, at a high-contrast edge, the smallest motion we can detect is on the order of 1/100th of a pixel (Fig. 1 and Fig. S4).

Results and Discussion

We applied the motion microscope to several problems in biology and engineering. First, we used it to reveal one component of the mechanics of hearing. The mammalian cochlea is a remarkable sensor that can perform high-quality spectral analysis to discriminate as many as 30 frequencies in the interval of a semitone (8). These extraordinary properties of the hearing organ depend on traveling waves of motion that propagate along the cochlear spiral. These wave motions are coupled to the extremely sensitive sensory receptor cells via the tectorial membrane, a gelatinous structure that is 97% water (9).

To better understand the functional role of the tectorial membrane in hearing, we excised segments of the tectorial membrane from a mouse cochlea and stimulated it with audio frequency vibrations (Movie S1 and Fig. 2*A*). Prior work suggested that motions of the tectorial membrane would rapidly decay with distance from the point of stimulation (10). The unprocessed video of the tectorial membrane appeared static, making it difficult to verify this. However, when the motions were amplified 20 times, waves that persisted over hundreds of micrometers were revealed (Movie S1 and Fig. 2 *B*–*E*).

Subpixel motion analysis suggests that these waves play a prominent role in determining the sensitivity and frequency selectivity of hearing (11–14). Magnifying motions has provided new insights into the underlying physical mechanisms of hearing.
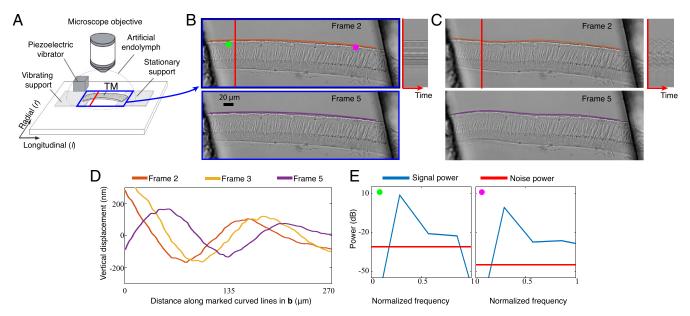

Fig. 2. Exploring the mechanical properties of a mammalian tectorial membrane with the motion microscope. (*A*) The experimental setup used to strobo-scopically film a stimulated mammalian tectorial membrane (*Tecta*[Y1870C/+]). Subfigure Copyright (2007) National Academy of Sciences of the United States of America. Reproduced from ref. 12. (*B*) Two of the eight captured frames . (Movie S1, data previously published in ref. 13). (*C*) Corresponding frames from the motion-magnified video in which displacement from the mean was magnified 20×. The orange and purple lines on top of the tectorial membrane in *B* are warped according to magnified motion vectors to produce the orange and purple lines in *C*. (*D*) The vertical displacement along the orange and purple lines in *B* is shown for three frames. (*E*) The power spectrum of the motion signal and noise power is shown in the direction of least variance at the magenta and green points in *B*.

Ultimately, the motion microscope could be applied to see and interpret the nanoscale motions of a multitude of biological systems.

We also applied the motion microscope to the field of modal analysis, in which a structure's resonant frequencies and mode shapes are measured to characterize its dynamic behavior (15). Common applications are to validate finite element models and to detect changes or damage in structures (16). Typically, this is done by measuring vibrations at many different locations on the structure in response to a known input excitation. However, approximate measurements can be made under operational conditions assuming broadband excitation (17). Contact accelerometers have been traditionally used for modal analysis, but densely instrumenting a structure can be difficult and tedious, and, for light structures, the accelerometers' mass can affect the measurement.

The motion microscope offers many advantages over traditional sensors. The structure is unaltered by the measurement, the measurements are spatially dense, and the motion-magnified video allows for easy interpretation of the motions. While only structural motions in the image plane are visible, this can be mitigated by choosing the viewpoint carefully.

We applied the motion microscope to modal analysis by filming the left span of a suspension bridge from 80 m away (Fig. 3A). The central span was lowered and impacted the left span. Despite this, the left span looks completely still in the input video (Fig. 3B). Two of its modal shapes are revealed in Movie S2 when magnified 400× (1.6 Hz to 1.8 Hz) and 250× (2.4 Hz to 2.7 Hz). In Fig. 3 C and D, we show time slices from the motion-magnified videos, displacements versus time at three points, and the estimated noise standard deviations. We also used accelerometers to measure the motions of the bridge at two of those points (Fig. 3B). The motion microscope matches the accelerometers within error bars. In a second example, we show the modal shapes of a pipe after it is struck with a hammer (*Modal Shapes of a Pipe*, Fig. S10, and Movie S3).

In our final example, we used the motion microscope to verify the functioning of elastic metamaterials, artificially structured materials designed to manipulate and control the propagation of elastic waves. They have received much attention (18) because of both their rich physics and their potential applications, which include wave guiding (19), cloaking (20), acoustic imaging (21), and noise reduction (22). Several efforts have been made to experimentally characterize the elastic wave phenomena observed in these systems. However, as the small amplitude of the propagating waves makes it impossible to directly visualize them, the majority of the experimental investigations have focused on capturing the band gaps through the use of accelerometers, which only provide point measurements. Visualizing the mechanical motions everywhere in the metamaterials has only been possible using expensive and highly specialized setups like scanning laser vibrometers (23).

We focus on a metamaterial comprising an elastic matrix with embedded resonating units, which consists of copper cores connected to four elastic beams (24). Even when vibrated, this metamaterial appears stationary, making it difficult to determine if the metamaterial is functioning correctly (Movies S4 and S5). Previously, these miniscule vibrations were measured with two accelerometers (24). This method only provides point measurements, making it difficult to verify the successful attenuation of vibrations. We gain insight and understanding of the system by visually amplifying its motion.
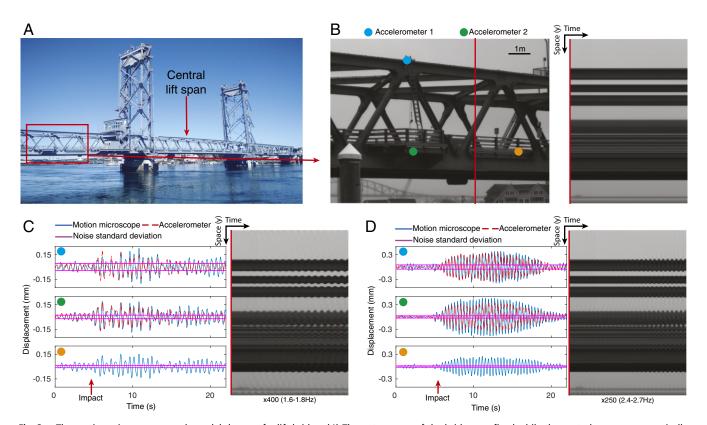

Fig. 3. The motion microscope reveals modal shapes of a lift bridge. (*A*) The outer spans of the bridge are fixed while the central span moves vertically. (*B*) The left span was filmed while the central span was lowered. A frame from the resulting video and a time slice at the red line are shown. (*C*) Displacement and noise SD from the motion microscope are shown for motions in a 1.6- to 1.8-Hz band at the cyan, green, and orange points in *B*. Doubly integrated data from accelerometers at the cyan and green points are also shown. A time-slice from the motion-magnified video is shown (Movie S2). The time at which the central span is fully lowered is marked as "impact." (*D*) Same as *C*, but for motions in a 2.4- to 2.7-Hz band.
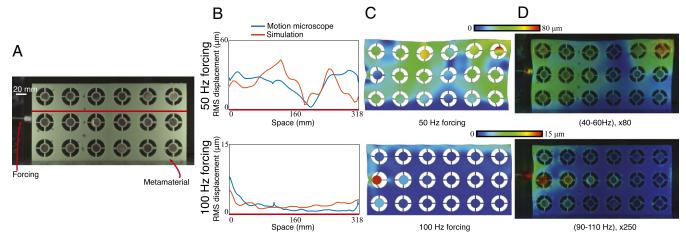
COMPUTER SCIENCES

Fig. 4. The motion microscope is used to investigate properties of a designed metamaterial. (*A*) The metamaterial is forced at 50 Hz and 100 Hz in two experiments, and a frame from the 50-Hz video is shown. (*B*) One-dimensional slices of the displacement amplitude along the red line in *A* are shown for both a finite element analysis simulation and the motion microscope. (*C*) A finite element analysis simulation of the displacement of the metamaterial. Color corresponds to displacement amplitude, and the material is warped according to magnified simulated displacement vectors. (*D*) Results from the motion microscope are shown. Displacement magnitudes are shown in color at every point on the metamaterial, overlaid on frames from the motion-magnified videos (Movies S4 and S5).

The elastic metamaterial was forced at two frequencies, 50 Hz and 100 Hz, and, in each case, it was filmed at 500 frames per second (FPS) (Fig. 4*A*). The motions in 20-Hz bands around the forcing frequencies were amplified, revealing that the metamaterial functions as expected (24), passing 50-Hz waves and rapidly attenuating 100-Hz waves (Movies S4 and S5). We also compared our results with predictions from a finite element analysis simulation (Fig. 4 *B* and *C*). In Fig. 4*D*, we show heatmaps of the estimated displacement amplitudes overlaid on the motion-magnified frames. We interpolated displacements into textureless regions, which had noisy motion estimates. The agreement between the simulation (Fig. 4*C*) and the motion microscope (Fig. 4*D*) demonstrates the motion microscope's usefulness in verifying the correct function of the metamaterial.

Conclusion

Small motions can reveal important dynamics in a system under study, or can foreshadow large-scale motions to come. Motion microscopy facilitates their visualization, and has been demonstrated here for motion amplification factors from 20× to 400× across length scales ranging from 100 nm to 0.3 mm.

Materials and Methods

Quantitative Motion Estimation. For every pixel at location (x, y) and time t, we combine spatial local phase information in different subbands of the frames of the input video using the least squares objective function,

$$\underset{u,v}{\arg\min} \sum_i A_{r_i,\theta_i}^2 \left[\left(\frac{\partial \phi_{r_i,\theta_i}}{\partial x}, \frac{\partial \phi_{r_i,\theta_i}}{\partial y} \right) \cdot (u, v) - \Delta \phi_{r_i,\theta_i} \right]^2. \qquad [2]$$

Arguments have been suppressed for readability; $A_{r_i,\theta_i}(x, y, t)$ and $\phi_{r_i,\theta_i}(x, y, t)$ are the spatial local amplitude and phase of a steerable pyramid representation of the image, and $u(x, y, t)$ and $v(x, y, t)$ are the horizontal and vertical motions, respectively, at every pixel. The solution ($\mathbf{V} = (u, v)$) is our motion estimate and is equal to

$$\mathbf{V} = (\mathbf{X}^T \mathbf{W} \mathbf{X})^{-1} (\mathbf{X}^T \mathbf{W} \mathbf{Y}), \qquad [3]$$

where $\mathbf{X}$ is $N \times 2$ with ith row $(\frac{\partial}{\partial x} \phi_{r_i,\theta_i}, \frac{\partial}{\partial y} \phi_{r_i,\theta_i})$, $\mathbf{Y}$ is $N \times 1$ with ith row $\Delta \phi_{r_i,\theta_i}$, and $\mathbf{W}$ is a diagonal $N \times N$ matrix with ith diagonal element A_{r_i,θ_i}^2.

To increase the signal-to-noise ratio, we assume the motion field is constant in a small window around each pixel. This gives additional constraints from neighboring pixels, weighted by both their amplitude squared and the corresponding value in a smoothing kernel K, to the objective described in Eq. **3**. To handle temporal filtering, we replace the local phase variations $\Delta \phi_{r,\theta}(x, y, t)$ with temporally filtered local phase variations.

We use a four-orientation complex steerable pyramid specified by Portilla and Simoncelli (25). We use only the two highest-frequency scales of the complex steerable pyramid, for a total of eight subbands. We use a Gaussian spatial smoothing kernel with a SD of 3 pixels and a support of 19×19 pixels. The temporal filter depends on the application.

Noise Model and Creating Synthetic Video. We estimate the noise level function (26) of a video. We apply derivative of Gaussian filters to the image in the x and y directions and use them to compute the gradient magnitude. We exclude pixels where the gradient magnitude is above 0.05 on a 0 to 1 intensity scale. At the remaining pixels, we take the temporal variance and mean of the image. We divide the intensity range into 64 equally sized bins. For each bin, we take all pixels with mean inside that bin and take the mean of the corresponding temporal variances of I to form 64 points that are linearly interpolated to estimate the noise level function f.

Estimating Covariance Matrices of Motion Vectors. For an input video $I(x, y, t)$, we use the noise level function f to create a synthetic video

$$I_S(x, y, t) = I_0(x, y, 0) + I_n(x, y, t)\sqrt{f(I_0(x, y, 0))} \qquad [4]$$

that is N frames long. We estimate the covariance matrices of the motion vectors by taking the temporal sample covariance of I_S,

$$\Sigma_{\mathbf{V}} = \frac{1}{N-1} \sum_t \left(\mathbf{V}_S(x, y, t) - \bar{\mathbf{V}}_S(x, y) \right) \left(\mathbf{V}_S(x, y, t) - \bar{\mathbf{V}}_S(x, y) \right)^T, \qquad [5]$$

where $\bar{\mathbf{V}}_S(x, y)$ is the mean over t of the motion vectors.

The temporal filter reduces noise and decreases the covariance matrix. Oppenheim and Schafer (27) show that a signal with independent and identically distributed (IID) noise of variance σ^2, when filtered with a filter with impulse response $T(t)$, has variance $\sum_t T(t)^2 \sigma^2$. Therefore, when a temporal filter is used, we multiply the covariance matrix by $\sum_t T(t)^2$.

Comparison of Our Motion Estimation to a Laser Vibrometer. We compare the results of our motion estimation algorithm to that of a laser vibrometer, which measures velocity using Doppler shift (28). In the first experiment, a cantilevered beam was shaken by a mechanical shaker at 7.3 Hz, 58.3 Hz, 128 Hz, and 264 Hz, the measured modal frequencies of the beam. The relative amplitude of the shaking signal was varied between a factor of 5 and 25 in 2.5 increments. We simultaneously recorded a 2,000 FPS video of the beam with a high-speed camera (VisionResearch Phantom V-10) and measured its horizontal velocity with a laser vibrometer (Polytec PDV100). We repeated this experiment for nine different excitation magnitudes, three focal lengths (24 mm, 50 mm, 85 mm) and eight exposure times (12.5 μs, 25 μs, 50 μs, 100 μs, 200 μs, 300 μs, 400 μs, 490 μs), for a total of 20 high-speed videos. The beam had an accelerometer mounted on it (white object in Fig. 1*A*), but we did not use it in this experiment.

We used our motion estimation method to compute the horizontal displacement of the marked, red point on the left side of the accelerometer from the video (Fig. 1*A*). We applied a temporal band-stop filter to remove motions between 67 Hz and 80 Hz that corresponded to camera motions caused by its cooling fan's rotation. The laser vibrometer signal was integrated using discrete, trapezoidal integration. Before integration, both signals were high-passed above 2.5 Hz to reduce low-frequency noise in the integrated vibrometer signal. The motion signals from each video were manually aligned. For one video (exposure, 490 μs; excitation, 25; and focal length, 85 mm), we plot the two motion signals (Fig. S4 *B–D*). They agree remarkably well, with higher modes well aligned and a correlation of 0.997.

To show the sensitivity of the motion microscope, we plot the correlation of our motion estimate and the integrated velocities from the laser vibrometer vs. motion size (RMS displacement). Because the motion's average size varies over time, we divide each video's motion signal into eight equal pieces and plot the correlations of each piece in each video in Fig. S4 *E and F*. For RMS displacements on the order of 1/100th of a pixel, the correlation between the two signals varies between 0.87 and 0.94. For motions larger than 1/20th of a pixel, the correlation is between 0.95 and 0.999. Possible sources of discrepancy are noise in the motion microscope signal, integrated low-frequency noise in the vibrometer signal, and slight misalignment between the signals. Displacements with RMS smaller than 1/100th of a pixel were noisier and had lower correlations, indicating that noise in the video prevents the two signals from matching.

As expected, correlation increases with focal length and excitation magnitude, two things that positively correlate with motion size (in pixels) (Fig. S4 *G and H*). The correlation also increases with exposure, because videos with lower exposure times are noisier (Fig. S4*I*).

Filming Bridge Sequence. The bridge was filmed with a monochrome Point Gray Grasshopper3 camera (model GS3-U3-23S6M-C) at 30 FPS with a resolution of 800 × 600. The central span of the bridge lifted to accommodate marine traffic. Filming was started about 5 s before the central span was lowered to its lowest point.

The accelerometer data were doubly integrated using trapezoidal integration to displacement. In Fig. 3 *C and D*, both the motion microscope displacement and the doubly integrated acceleration were band-passed with a first-order band-pass Butterworth filter with the specified parameters.

Motion Field Interpolation. In textureless regions, it may not be possible to estimate the motion at all, and, at one-dimensional structures like edges, the motion field will only be accurate in the direction perpendicular to the edge. These inaccuracies are reflected in the motion covariance matrix. We show how to interpolate the motion field from accurate regions to inaccurate regions, assuming that adjacent pixels have similar motions.

We minimize the following objective function:

$$\sum_{\mathbf{x}} (\mathbf{V}_S(\mathbf{x}) - \mathbf{V}(\mathbf{x}))\Sigma_{\mathbf{V}}^{-1}(\mathbf{x})(\mathbf{V}_S(\mathbf{x}) - \mathbf{V}(\mathbf{x}))^T +$$

$$\lambda_S \sum_{\mathbf{y} \in \mathcal{N}(\mathbf{x})} (\mathbf{V}_S(\mathbf{x}) - \mathbf{V}_S(\mathbf{y}))(\mathbf{V}_S(\mathbf{x}) - \mathbf{V}_S(\mathbf{y}))^T, \qquad [6]$$

where $\mathbf{V}_S$ is the desired interpolated field, $\mathbf{V}$ is the estimated motion field, $\Sigma_{\mathbf{V}}$ is its covariance, $\mathcal{N}(\mathbf{x})$ is the four-pixel neighborhood of x, and λ_S is a user-specified constant that specifies the relative importance of matching the estimated motion field vs. making adjacent pixels have similar motion fields. The first term seeks to ensure that $\mathbf{V}_S$ is close to $\mathbf{V}$, weighted by the expected amount of noise at each pixel. The second term seeks to ensure that adjacent pixels have similar motion fields.

In Fig. 4*D*, we produce the color overlays by applying the above processing to the estimated motion field with $\lambda_S = 300$ and then taking the amplitude of each motion vector. We also set components of the covariance matrix that were larger than 0.1 square pixels to be an arbitrarily large number (we used 10,000 square pixels).

Finite Element Analysis of Acoustic Metamaterial. We use Abaqus/Standard (29), a commercial finite-element analyzer, to simulate the metamaterial's response to forcing. We constructed a 2D model with 37,660 nodes and 11,809 eight-node plane strain quadrilateral elements (Abaqus element type CPE8H). We modeled the rubber as Neo-Hookean, with shear modulus 443.4 kPa, bulk modulus 7.39×10^5 kPa, and density 1,050 kg·m^3 (Abaqus parameters C10 = 221.7 kPa, D1 = 2.71×10^{-9} Pa^{-1}). We modeled the copper core with shear modulus 4.78×10^7 kPa, bulk modulus $1.33 \times^8$ kPa, and density 8,960 kg·m^3 (Abaqus parameters C10 = 2.39×10^7 kPa, D1 = 1.5×10^{-11} Pa^{-1}). Geometry and material properties are specified in Wang et al. (24). The bottom of the metamaterial was given a zero-displacement boundary condition. A sinusoidal displacement loading condition at the forcing frequency was applied to a node located halfway between the top and bottom of the metamaterial.

Validation of Noise Analysis with Real Video Data. We took a video of an accelerometer attached to a beam (Fig. S9*A*). We used the accelerometer to verify that the beam had no motions between 600 Hz and 700 Hz (Fig. S9*B*). We then estimated the in-band motions from a video of the beam. Because the beam is stationary in this band, these motions are entirely due to noise, and their temporal sample covariance gives us a ground-truth measure of the noise level (Fig. S9*C*). We used our simulation with a signal-dependent noise model to estimate the covariance matrix from the first frame of the video, the specific parameters of which are shown in Fig. S9*D*. The resulting covariance matrices closely match the ground truth (Fig. S9 *E and F*), showing that our simulation can accurately estimate noise level and error bars.

We also verify that the signal-dependent noise model performs better than the simpler constant variance noise model, in which noise is IID. The result of the constant noise model simulation produced results that are much less accurate than the signal-dependent noise model (Fig. S9 *G and H*).

In Fig. S9, we only show the component of the covariance matrix corresponding to the direction of least variance, and only at points corresponding to edges or corners.

1. Liu C, Torralba A, Freeman WT, Durand F, Adelson EH (2005) Motion magnification. *ACM Trans Graph* 24:519–526.
2. Wu HY, et al. (2012) Eulerian video magnification for revealing subtle changes in the world. *ACM Trans Graph* 31:1–8.
3. Wadhwa N, Rubinstein M, Durand F, Freeman WT (2013) Phase-based video motion processing. *ACM Trans Graph* 32:80.
4. Wadhwa N, Rubinstein M, Durand F, Freeman WT (2014) Riesz pyramid for fast phase-based video magnification. *IEEE International Conference on Computational Photography* (Inst Electr Electron Eng, New York), pp 1–10.
5. Nakamura J (2005) *Image Sensors and Signal Processing for Digital Still Cameras* (CRC, Boca Raton, FL).
6. Simoncelli EP, Freeman WT (1995) The steerable pyramid: A flexible architecture for multi-scale derivative computation. *Int J Image Proc* 3:444–447.
7. Fleet DJ, Jepson AD (1990) Computation of component image velocity from local phase information. *Int J Comput Vis* 5:77–104.
8. Dallos P, Fay RR (2012) *The Cochlea,* Springer Handbook of Auditory Research (Springer Science, New York), Vol 8.
9. Thalmann I (1993) Collagen of accessory structures of organ of Corti. *Connect Tissue Res* 29:191–201.
10. Zwislocki JJ (1980) Five decades of research on cochlear mechanics. *J Acoust Soc Am* 67:1679–1685.
11. Sellon JB, Farrahi S, Ghaffari R, Freeman DM (2015) Longitudinal spread of mechanical excitation through tectorial membrane traveling waves. *Proc Natl Acad Sci USA* 112:12968–12973.
12. Ghaffari R, Aranyosi AJ, Freeman DM (2007) Longitudinally propagating traveling waves of the mammalian tectorial membrane. *Proc Natl Acad Sci USA* 104:16510–16515.
13. Sellon JB, Ghaffari R, Farrahi S, Richardson GP, Freeman DM (2014) Porosity controls spread of excitation in tectorial membrane traveling waves. *J Biophys* 106:1406–1413.
14. Ghaffari R, Aranyosi AJ, Richardson GP, Freeman DM (2010) Tectorial membrane traveling waves underlie abnormal hearing in tectb mutants. *Nat Commun* 1:96.
15. Ewins DJ (1995) *Modal Testing: Theory and Practice*, Engineering Dynamics Series (Res Stud, Baldock, UK) Vol 6.
16. Salawu O (1997) Detection of structural damage through changes in frequency: A review. *Eng Struct* 19:718–723.
17. Hermans L, van der Auweraer H (1999) Modal testing and analysis of structures under operational conditions: Industrial applications. *Mech Sys Signal Process* 13:193–216.
18. Hussein MI, Leamy MJ, Ruzzene M (2014) Dynamics of phononic materials and structures: Historical origins, recent progress, and future outlook. *Appl Mech Rev* 66:040802.
19. Khelif A, Choujaa A, Benchabane S, Djafari-Rouhani B, Laude V (2004) Guiding and bending of acoustic waves in highly confined phononic crystal waveguides. *Appl Phys Lett* 84:4400–4402.

COMPUTER SCIENCES

20. Cummer S, Schurig D (2007) One path to acoustic cloaking. *New J Phy* 9:45.
21. Spadoni A, Daraio C (2010) Generation and control of sound bullets with a nonlinear acoustic lens. *Proc Natl Acad Sci USA* 107:7230–7234.
22. Elser D, et al. (2006) Reduction of guided acoustic wave Brillouin scattering in photonic crystal fibers. *Phys Rev Lett* 97:133901.
23. Jeong S, Ruzzene M (2005) Experimental analysis of wave propagation in periodic grid-like structures. *Proc SPIE* 5760:518–525.
24. Wang P, Casadei F, Shan S, Weaver JC, Bertoldi K (2014) Harnessing buckling to design tunable locally resonant acoustic metamaterials. *Phys Rev Lett* 113: 014301.
25. Portilla J, Simoncelli EP (2000) A parametric texture model based on joint statistics of complex wavelet coefficients. *Int J Comput Vis* 40:49–70.
26. Liu C, Freeman WT, Szeliski R, Kang SB (2006) Noise estimation from a single image. *2006 IEEE Computer Society Conference on Computer Vision and Pattern Recognition* (Inst Electr Electron Eng, New York), pp 901–908.
27. Oppenheim AV, Schafer RW (2010) *Discrete-Time Signal Processing* (Prentice Hall, New York).
28. Durst F, Melling A, Whitelaw JH (1976) *Principles and Practice of Laser-Doppler Anemometry.* NASA STI/Recon Technical Report A (NASA, Washington, DC), Vol 76.
29. Hibbett, Karlsson, Sorensen (1998) *ABAQUS/Standard: User's Manual* (Hibbitt, Karlsson & Sorensen, Pawtucket, RI) Vol 1.
30. Blaber J, Adair B, Antoniou A (2015) Ncorr: Open-source 2D digital image correlation MATLAB software. *Exp Mech* 55:1105–1122.
31. Xu J, Moussawi A, Gras R, Lubineau G (2015) Using image gradients to improve robustness of digital image correlation to non-uniform illumination: Effects of weighting and normalization choices. *Exp Mech* 55:963–979.
32. Unser M (1999) Splines: A perfect fit for signal and image processing. *Signal Process Mag* 16:22–38.
33. Fleet DJ (1992) *Measurement of Image Velocity* (Kluwer Acad, Norwell, MA).
34. Hasinoff SW, Durand F, Freeman WT (2010) Noise-optimal capture for high dynamic range photography. *2010 IEEE Computer Society Conference on Computer Vision and Pattern Recognition* (Inst Electr Electron Eng, New York), pp 553–560.
35. Lucas BD, Kanade T (1981) An iterative image registration technique with an application to stereo vision. *Int Joint Conf Artif Intell* 81:674–679.
36. Horn B, Schunck B (1981) Determining optical flow. *Artif Intell* 17:185–203.
37. Wadhwa N, et al. (2016) Eulerian video magnification and analysis. *Commun ACM* 60:87–95.
38. Wachel JC, Morton SJ, Atkins KE (1990) Piping vibration analysis. *Proceedings of the 19th Turbomachinery Symposium*, pp 119–134.